Design of Virtual Synchronous Generators with Enhanced Frequency Regulation and Reduced Voltage Distortions

Jingyang Fang, Xiaoqiang Li, Yi Tang
School of Electrical and Electronic Engineering
Nanyang Technological University
Singapore
E-mail: jfang006@e.ntu.edu.sg, lixiaoqiang@ntu.edu.sg, yitang@ntu.edu.sg

Hongchang, Li
Energy Research Institute @ NTU (ERI@N)
Nanyang Technological University
Singapore
E-mail: hongchangli@ntu.edu.sg

***Abstract*— In modern power systems where the penetration of renewable energy resources is normally high, functions of voltage and frequency support are supposed to be taken over by virtual synchronous generators (VSGs) or virtual synchronous machines (VSMs), i.e., grid-connected inverters which are controlled to mimic the terminal characteristics of synchronous generators. In this paper, the comprehensive design of VSGs is provided in detail. The proposed control scheme consists of two control loops. The inner-loop voltage and current controller is designed in the discrete *z*-domain to guarantee system stability and voltage control with low distortions, while the design of the outer-loop frequency and power controller is performed in the continuous *s*-domain to be in consistence with the conventional power system frequency regulation models. With the proposed design method, various control objectives, e.g., resonance damping, voltage support, primary frequency regulation, secondary frequency regulation, and virtual inertia, can easily be achieved and evaluated. Finally, experimental results obtained from a 500-W three-phase virtual synchronous generator prototype are presented to verify the effectiveness of the proposed design method.**

Keywords—Frequency regulation; Power converter; virtual synchronous generator (VSG); virtual synchronous machine (VSM); voltage support

I. INTRODUCTION

Renewable energy resources have been deployed in a large scale due to their echo-friendly feature and the increasing worldwide energy demand, and this has reshaped the paradigm of modern power systems [1]. Previously, synchronous generators possessing rotational inertia are responsible for voltage and frequency support. Nowadays, renewable generators, e.g., solar photovoltaic (PV) arrays and wind turbines, are employed to gradually replace synchronous generators. Generally, such distributed generators are coupled to the power grid through fast-response power converters. In most cases, however, these power converters are controlled as current sources to extract the maximum power from primary energy sources without providing any inertia or frequency/voltage support [1−3]. As a result, frequency deviations may easily go beyond the acceptable range and cause instability issues for systems with high penetration of renewable energy resources [4]. Moreover, the operations of islanded microgrids become particularly an issue, because few generators are in charge of frequency or voltage support [3].

To achieve the objective of renewable integration, grid-connected inverters can be controlled in such a way that their terminal characteristics are the same as synchronous generators. This concept, known as virtual synchronous generators (VSGs) [5], virtual synchronous machines (VSMs) [6], or synchronverters [7], has received increasing attentions. In [6], the experimental results indicate that VSGs exhibit similar responses as synchronous generators under voltage and frequency disturbances. However, it lacks detailed descriptions of the control structure and system parameter values. Moreover, an approximate 100 μs execution time for the presented single-phase VSG algorithm would prohibit it from further adaptation to three-phase systems [6]. As a milestone, the mathematical model of VSGs covers all the dynamics of synchronous generators has been established in [7], where accurate power regulation and load sharing among power converters are supposed to be achieved. Nonetheless, the model of the output *LC* filter is excluded from the analysis, which means that potential resonance and instability issues have been ignored. In addition, since the presented model focuses deeply on synchronous generators, numerous mathematical calculations and complicated control structures are inevitable.

Actually, as recently reported in [8−11], it is not necessary to incorporate all the electrical and mechanical components of synchronous generators into the model of VSGs. Under most circumstances, only the equations describing the power and frequency/voltage interaction behaviors of synchronous generators should be taken into account, as they describe the essential functions of inertia emulation and frequency/voltage support. Among these equations, it has been identified that the swing equation is the most critical one, and its effect can be emulated by grid-connected inverters when equipped with low-pass-filtered droop-based control schemes [8]. Based on this understanding, extensive performance comparisons between VSGs and droop-based inverters are performed to emphasize their differences and similarities in [9]. Detailed small-signal models of VSGs are constructed in [9] and [10] to validate

978-1-5386-1180-7/18/$31.00 ©2018 IEEE

their respective points. Although these models are rigorously derived step-by-step from the swing equation, they are still very different from the conventional power system frequency regulation models, making it difficult for modern power systems to inherit the analysis and control methods used in traditional power systems. Additionally, the complete design of controllers is beyond the scope of these references. To fill these gaps, this paper provides an instruction for designing high-performance VSGs with enhanced frequency regulation and reduced voltage distortions.

II. System Description

Fig. 1 presents the overall schematic diagram of the VSG system. As seen, the power circuit of the VSG consists of a three-phase power converter and an output *LC* filter. The fundamental objective of the VSG is to provide voltage support, namely the regulation of the amplitudes and phases of AC output voltages v_{cx} (x = a, b, c). This objective can be achieved through adopting the inner-loop voltage/current controller. In this sense, the VSG can be regarded as a controllable voltage source. Furthermore, the output frequency and power of the VSG should be adjusted correspondingly to the change of system operating conditions so as to provide frequency support and system inertia. The outer-loop frequency/power controller allows the realization of these functions. Although the phase-locked-loop (PLL) can be removed from the VSG control, as indicated by [12], this necessitates accurate measurement of the grid impedance, and thus, the PLL is employed in this study to provide information of system frequency.

In the following sections, the proposed controllers will be designed separately according to their relevant time-scales. For the voltage/current controller, the discrete z-domain model is preferable, since it provides accurate information for evaluating the stability conditions of voltage/current control. In contrast, the slow response of the frequency/power controller allows it to be designed in the continuous s-domain, which is in consistence with the conventional frequency regulation models. These controllers will be designed based on the system parameter values listed in Table I.

III. Design of Voltage/Current Controller

In this section, the voltage/current controller will be designed step by step based on the mathematic model derived in the discrete z-domain.

A. Modelling VSG in dq0-frame

Let $v_{xN}(t)$ (x = A, B, C) denotes the voltage between the node x and node N. According to the Kirchhoff's voltage law (KVL), the following differential equations can be obtained:

$$\begin{cases} v_{AN}(t) = v_{ca}(t) + L_i \dfrac{di_{ia}(t)}{dt} + v_{N'N}(t) \\ v_{BN}(t) = v_{cb}(t) + L_i \dfrac{di_{ib}(t)}{dt} + v_{N'N}(t) \\ v_{CN}(t) = v_{cc}(t) + L_i \dfrac{di_{ic}(t)}{dt} + v_{N'N}(t) \end{cases}. \quad (1)$$

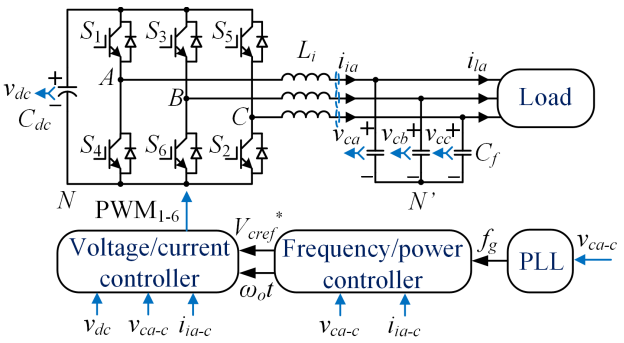

Fig. 1. Schematic diagram of a virtual synchronous generator system.

Table I. System parameter values.

Description	Symbol	Value
Filter capacitance	C_f	50 μF
Filter inductance	L_i	1 mH
DC-link capacitance	C_{dc}	2.82 mF
DC-link voltage	V_{dc}	200 V
Voltage reference rms	V_{cref}	50 V
Active power reference	P_{ref}	500 W
Frequency reference	f_{ref}	50 Hz

For balanced three-phase systems, the sum of three-phase voltages or three-phase currents is always zero. Summing the three equations in (1), and then $v_{N'N}(t)$ = 1/3[$v_{AN}(t)$ + $v_{BN}(t)$ $v_{CN}(t)$] can be obtained. Let $v_{xN}(t)$ = $V_{dc}S_x(t)$ (x = A, B, C), where $S_x(t)$ denotes the switch function. When $S_x(t)$ = 1, the upper switch turns on, and the lower switch turns off. In contrast, when $S_x(t)$ = 0, the operation of these two switches are exchanged. Through using the above alternative expressions and the following *abc* to *dq*0 transformation matrix [13]:

$$T_{abc-dq0} = \frac{2}{3}\begin{bmatrix} \cos\omega_o t & \cos(\omega_o t - \frac{2\pi}{3}) & \cos(\omega_o t + \frac{2\pi}{3}) \\ -\sin\omega_o t & -\sin(\omega_o t - \frac{2\pi}{3}) & -\sin(\omega_o t + \frac{2\pi}{3}) \\ \frac{1}{2} & \frac{1}{2} & \frac{1}{2} \end{bmatrix}, \quad (2)$$

the system plant can be expressed in the *dq*0-frame as:

$$\begin{cases} V_{dc}S_d(t) = v_{cd}(t) + L_i \dfrac{di_{id}(t)}{dt} - \omega_o L_i i_{iq}(t) \\ V_{dc}S_q(t) = v_{cq}(t) + L_i \dfrac{di_{iq}(t)}{dt} + \omega_o L_i i_{id}(t) \\ V_{dc}S_0(t) = v_{c0}(t) + L_i \dfrac{di_{i0}(t)}{dt} \end{cases}. \quad (3)$$

Note that the 0-axis components in (3) are always zero for balanced three-phase systems, and hence, they are ignored here. It is clear from (3) that there exist coupling terms, namely

$-\omega_o L_i i_{iq}(t)$ and $\omega_o L_i i_{id}(t)$, between the *d*- and *q*-axis. It is possible to eliminate such coupling effects through using the relevant feed-forward terms, as demonstrated in Fig. 2. After the decoupling of the *d*- and *q*- axis, the voltage/current controller can be designed independently on the *d*- and *q*- axis.

The overall structure of the voltage/current controller is shown in Fig. 3, where $G_f(z)$ and $G_v(z)$ respectively denote the voltage feed-forward term and voltage compensator, $G_i(z)$ and D_{lf} respectively stand for the current compensator and current feedback gain, and K_{PWM} represents the gain of the pulse-width-modulator (PWM). K_{PWM} is selected as one in this study, because its effect can be implemented by modifying the control parameters of the other blocks. Transfer functions of the one sampling period delay and zero-order-hold, denoted as z^{-1} and ZOH in Fig. 3, are introduced by the PWM calculation and reference update, respectively [2]. Since this control structure is applicable to both the *d*- and *q*-axis, the relevant notations of *d* and *q* are omitted in Fig. 3. As mentioned, the primary objective of the voltage/current controller is to regulate its output voltages v_{cx} ($x = d, q$) to track their references v_{cref_x} ($x = d, q$), and these references are represented as:

$$\begin{aligned} v_{cref\_d}(z) &= V_{cref}^{*} \\ v_{cref\_q}(z) &= 0, \end{aligned} \tag{4}$$

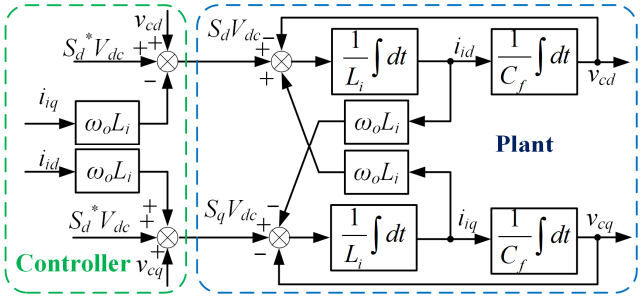

Fig. 2. Block diagram for decoupling of the *d*- and *q*-axis.

where V_{cref}^{*} is the reference voltage obtained from the first output of the frequency/power controller (See Fig. 1). In the following subsection, the inner-loop current controller will first be designed.

B. Design of current controller

The functions of the current controller include limiting the converter current and damping of the resonance introduced by the *LC* filter. To implement these functions, the inductor current i_i should track its reference i_{iref} as fast and accurate as possible. For a well-designed current controller, the disturbance caused by the load current $i_l(s)$ can be neutralized by the feed-forward term $i_l(z)$ at the expense of three additional current sensors. Ignoring the effect of i_l, and the transfer functions from $v_{inv}(s)$ to $i_i(s)$ and $v_c(s)$ can respectively be derived as follows:

$$v_{inv\_i}(s) = \frac{C_f s}{L_i C_f s^2 + 1}. \tag{5}$$

$$v_{inv\_v}(s) = \frac{1}{L_i C_f s^2 + 1}. \tag{6}$$

Considering the effect of ZOH, (5) and (6) can further be expressed in the *z*-domain as:

$$v_{inv\_i}(z) = \frac{(z-1)\sin\omega_r T_s}{L_i\omega_r\left(z^2 - 2z\cos\omega_r T_s + 1\right)}, \tag{7}$$

$$v_{inv\_v}(z) = \frac{(1+z)(1-\cos\omega_r T_s)}{z^2 - 2z\cos\omega_r T_s + 1}, \tag{8}$$

where $\omega_r = 1 / (L_i C_f)^{1/2}$ denotes the resonance frequency of the *LC* filter. Using (7) and (8), it is possible to derive the discrete block diagram of the voltage/current, as shown in Fig. 4. Although the current controller serves to damp the resonance,

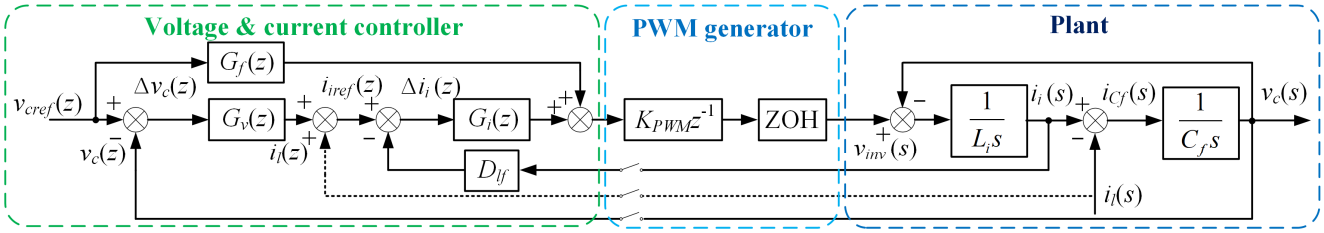

Fig. 3. Block diagram of the voltage/current controller.

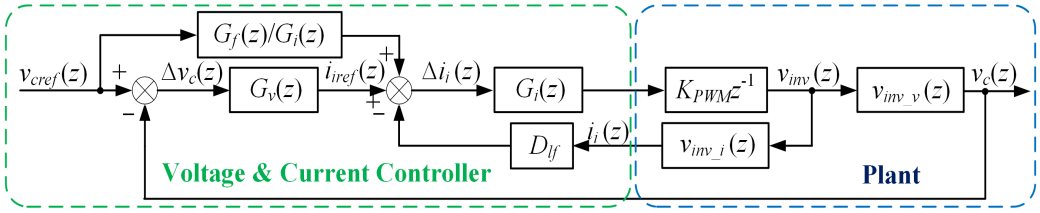

Fig. 4. Discrete block diagram of the voltage/current controller in the *z*-domain.

$$T_{iref\_v}(z) = \frac{G_i(z)K_{PWM}L_i\omega_r(1-\cos\omega_r T_s)(1+z)}{z\left(z^2 - 2z\cos\omega_r T_s + 1\right)L_i\omega_r + D_{Lf}G_i(z)K_{PWM}\sin\omega_r T_s\,(z-1)}. \tag{9}$$

its ultimate objective is to improve the performances of voltage control. Therefore, the transfer function from $i_{iref}(z)$ to $v_c(z)$, denoted as $T_{iref\_v}(z)$, will be evaluated instead of that from $i_{iref}(z)$ to $i_i(z)$. $T_{iref\_v}(z)$ can be derived from Fig. 4 and listed in (9) shown at the bottom of the previous page. It is clear from (9) that the poles of $T_{iref\_v}(z)$ are influenced by the product of D_{lf} and $G_i(z)$. To simplify the design, $G_i(z)$ is selected to be a proportional controller with a gain K_i. Under this assumption, the zero-pole map of $T_{iref\_v}(z)$ with various products of K_i and D_{lf} is shown in Fig. 5. As observed, the employment of the current controller shifts the poles of $T_{iref\_v}(z)$. With the increase of $D_{lf}K_i$, the inner-loop gradually becomes stabilized, and then it becomes unstable again. When $D_{lf}K_i = 4$, the system exhibits the best damping effect, as the conjugate poles are located closest to the origin of the unit cycle.

When deriving the steady state gain of $T_{iref\_v}(z)$, the second term of its denominator becomes 0 as z is equal to one in the steady-state. Therefore, the steady state gain is solely determined by $G_i(z)$ or K_i, and D_{lf} has no effect on it. The respective impact of K_i and D_{lf} can be visualized by the step response diagrams of $T_{iref\_v}(z)$ illustrated in Fig. 6. It is noted that an increased steady state gain can be obtained with a larger K_i. However, it remains unchanged as D_{lf} varies. Among all the cases, the case of ($D_{lf} = 4$, $K_i = 1$) gives the lowest overshoot and recovery time as well as the unity steady state gain.

The Bode diagrams of $T_{iref\_v}(z)$ with and without the current feedback are shown in Fig. 7. As seen, without the current feedback ($D_{lf} = 0$, $K_i = 1$), there is an observable resonant peak introduced by the LC filter. After employing the current feedback, this resonant peak can effectively be damped, leading to a unity gain within a wide frequency band ranges from 100 Hz to 1.3 kHz. This characteristic is desired for designing the voltage controller. In the following analysis, the current controller together with the system plant will be simplified as $T_{iref\_v}(z)$.

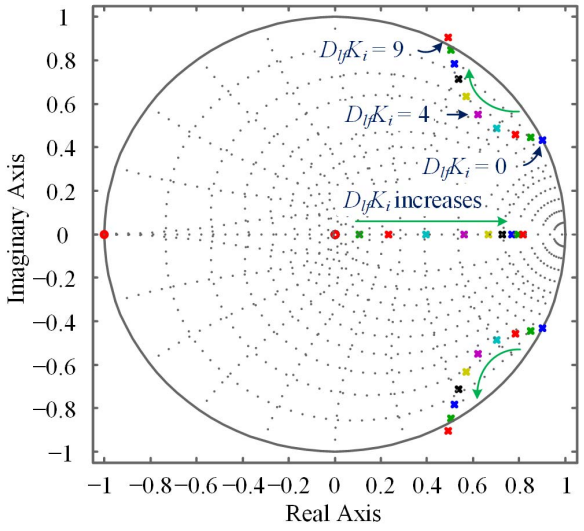

Fig. 5. Zero-pole map of $T_{iref\_v}(z)$ with various products of K_i and D_{lf}.

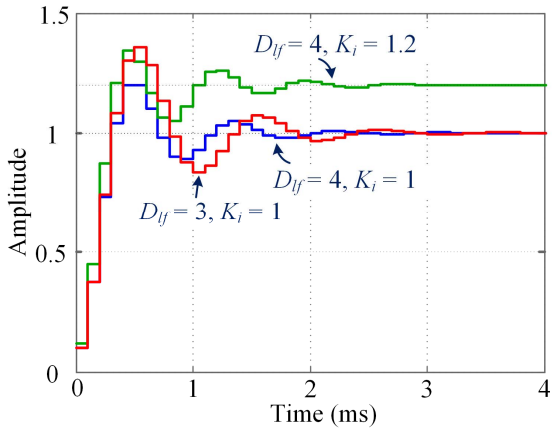

Fig. 6. Step responses of $T_{iref\_v}(z)$ with various K_i and D_{lf}.

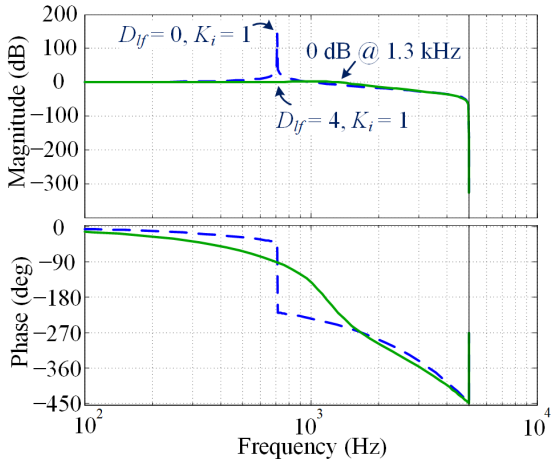

Fig. 7. Bode diagrams of $T_{iref\_v}(z)$ with $D_{lf} = 4$ and $D_{lf} = 0$.

C. Design of voltage controller

The voltage controller aims to minimize the steady state error and achieve disturbance rejection. In this subsection, the voltage controller $G_v(z)$ will be carefully designed. Normally, the voltage feed-forward term $G_f(z)$ shown in Fig. 3 is selected to be one so as to cancel with the disturbance caused by v_c. To reject the harmonic disturbances while reducing the steady state error at f_{ref}, a repetitive controller shunted with an integral controller $K_{vi}(z)$ is employed as the voltage controller $G_v(z)$, and its control structure is shown in Fig. 8. As observed, the repetitive controller consists of a fundamental period delay unit z^{-N_r}, a close to unity constant or low-pass filter $Q(z)$, a phase lead unit $z^{k_{rp}}$, a low-pass filter $S(z)$, and a gain K_r [14].

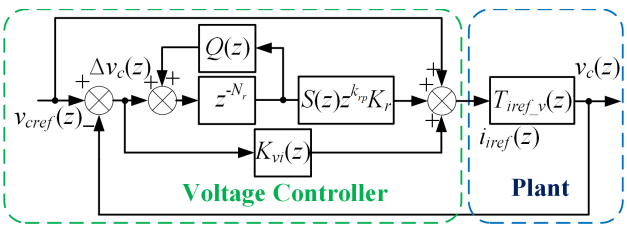

Fig. 8. Block diagram of the voltage controller $G_v(z)$.

First of all, the repetitive controller is designed while the integrator $K_{vi}(z)$ is ignored. In this case, the error $\Delta v_c(z)$ can be expressed as:

$$\Delta v_c(z) = \frac{v_{cref}(z)\left[z^{N_r} - Q(z)\right]\left[1 - T_{iref\_v}(z)\right]}{S(z)z^{k_{rp}}K_r T_{iref\_v}(z) + z^{N_r} - Q(z)}. \quad (10)$$

The denominator of (10) represents the system characteristic equation. For a stable system, every root of its characteristic equation should be inside the unit cycle. A sufficient condition for this prerequisite is expressed as:

$$\left|H(z)\right|_{z=e^{j\omega T_s}} = \left|Q(z) - S(z)z^{k_{rp}}K_r T_{iref\_v}(z)\right|_{z=e^{j\omega T_s}} < 1. \quad (11)$$

The steady state errors at the harmonic frequencies can be obtained by replacing z with $e^{j2k\pi / N_r}$ (k = 1, 2, 3…) in (10), which can be expressed as:

$$\left|\Delta v_c(z)\right|_{z=e^{j2k\pi/Nr}} = \left|\frac{v_{cref}(z)\left[1 - Q(z)\right]\left[1 - T_{iref\_v}(z)\right]}{1 - H(z)}\right|_{z=e^{j2k\pi/Nr}}. \quad (12)$$

It can be noticed from (12) that the errors will be minimized as $Q(z)$ and $T_{iref\_v}(z)$ approach one at harmonic frequencies. In addition, $|H(z)|$ should be far from one to avoid the undesirable harmonics amplification. Based on these considerations, the repetitive controller can be designed step by step as follows:

1) Design of $S(z)$: the function of $S(z)$ is to provide sufficient attenuations in the high frequency domain. To guarantee sufficient attenuations, $S(z)$ is selected to be a second-order infinite-impulse-response (IIR) Butterworth low-pass filter with a cut-off frequency of 500 Hz. It should be noted that the cut-off frequency of the IIR filter is not equivalent to the bandwidth of the voltage controller, because the repetitive controller may boost the magnitude of the system loop gain. With $S(z)$ selected, the magnitude diagram of $T_{iref\_v}(z)S(z)$ is shown in Fig. 9.

2) Design of z^{krp}: the function of z^{krp} is to compensate for the phase lag in $T_{iref\_v}(z)S(z)$. As observed from Fig. 9, k_{rp} = 6 gives a zero phase-shift up to 1.3 kHz, which is higher than the other cases, and therefore, it is selected here.

3) Design of N_r, $Q(z)$, and K_r: N_r can easily be determined by the ratio of the switching frequency f_s and fundamental frequency f_{ref}. Since the magnitude of $T_{iref\_v}(z)S(z)z^{krp}$ is already 0 dB in the low frequency domain, K_r is selected to be one. $Q(z)$ can be chosen as a constant around one, and it should be less than one to guarantee the system stability. Finally, $Q(z)$ is selected to be 0.95 in this study.

Based on the above analysis, the Bode diagram of the

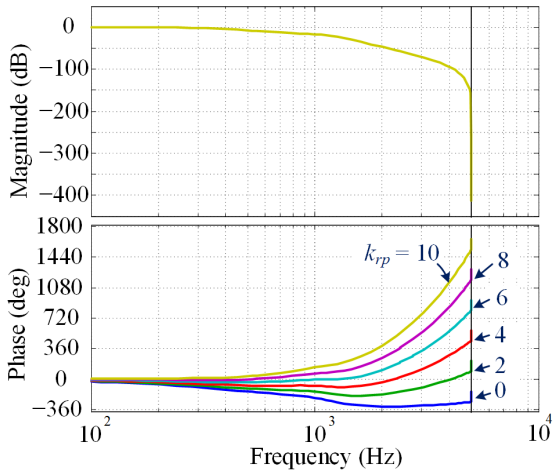

Fig. 9. Bode diagrams of $T_{iref\_v}(z)S(z)z^{krp}$.

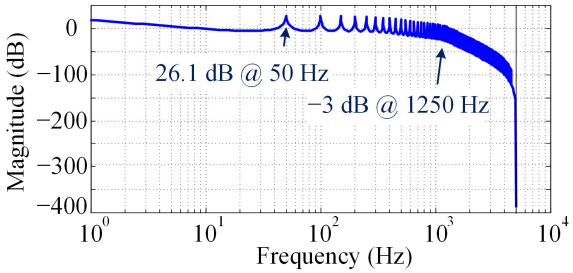

Fig. 10. Bode diagram of $v_c(z)$ / $\Delta v_c(z)$.

system loop gain, i.e., $v_c(z)$ / $\Delta v_c(z)$, is depicted in Fig. 10. As observed, it exhibits strong attenuations at the harmonic frequencies. Besides, the control bandwidth is around 1250 Hz, which is much larger than the cut-off frequency of $S(z)$.

To eliminate the steady state error of voltage control, an integrator can be shunted with the repetitive controller. Considering the effect of $K_{vi}(z)$, the error $\Delta v_c(z)$ should be reorganized as (13), and the relevant stability requirement is changed into (14), as shown at the bottom of this page. Assuming that the system is stable with the integrator alone, in other words, the roots of 1 + $K_{vi}(z)T_{iref\_v}(z)$ are inside the unit cycle. The stability of the system with the integrator can be evaluated by replacing $T_{iref\_v}(z)$ in (11) with $T_{iref\_v}(z)$ / [1+ $T_{iref\_v}(z)K_{vi}(z)$] in (14), where $K_{vi}(z)$ can be expressed as:

$$K_{vi}(z) = \frac{K_{vi}T_s(z+1)}{2(z-1)}. \quad (15)$$

With the integral gain K_{vi} = 70, the Nyquist diagram of $S(z)z^{krp}K_r T_{iref\_v}(z)$ / [1 + $T_{iref\_v}(z)K_{vi}(z)$] is illustrated in Fig. 11. As seen, with the increase of ω, the phase of $S(z)z^{krp}K_r T_{iref\_v}(z)$ /

$$\Delta v_c(z) = \frac{v_{cref}(z)\left[z^{N_r} - Q(z)\right]\left[1 - T_{iref\_v}(z)\right]}{\left[S(z)z^{k_{rp}}K_r - K_{vi}(z)Q(z)\right]T_{iref\_v}(z) + z^{N_r}\left[1 + K_{vi}(z)T_{iref\_v}(z)\right] - Q(z)}. \quad (13)$$

$$\left|H(z)\right|_{z=e^{j\omega T_s}} = \left|Q(z) - \frac{S(z)z^{k_{rp}}K_r T_{iref\_v}(z)}{1 + K_{vi}(z)T_{iref\_v}(z)}\right|_{z=e^{j\omega T_s}} < 1. \quad (14)$$

[1 + $T_{iref\_y}(z)K_{vi}(z)$] gradually approaches 180 degrees, leading it toward the boundary of the unit cycle. Fortunately, the magnitude has already been well attenuated by $S(z)$, as verified by Fig. 9. It is clear from Fig. 11 that the system is stable, because $H(z)$ is always located inside the unit cycle. Table II summarizes the parameters of the voltage/current controller.

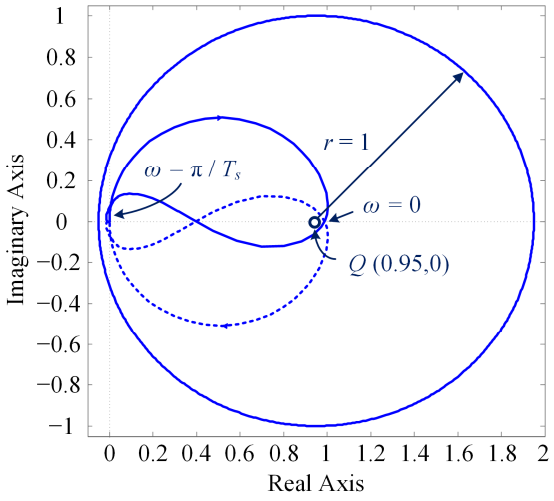

Fig. 11. Nyquist diagram of $S(z)z^{k_{rp}}K_rT_{iref\_y}(z) / [1 + T_{iref\_y}(z)K_{vi}(z)]$.

Table II. Voltage/current controller parameter values.

Description	Symbol	Value
Current controller gain	$G_i(z) / K_i$	1
Current feedback coefficient	D_{if}	4
Feed-forward coefficient	$G_f(z)$	1
Delay number	N_r	200
Stabilization factor	$Q(z)$	0.95
Phase compensation factor	k_{pr}	6
Integral gain	K_{vi}	70
Repetitive controller gain	K_r	1
Cut-off *f* of low-pass filter	f_c	500 Hz
Switching frequency	f_s	10 kHz
Fundamental frequency	f_{ref}	50 Hz

IV. Deisgn of Frequency/Power Controller

The objectives of the frequency/power controller include frequency support and inertia emulation. Its control structure is demonstrated in Fig. 12, where the active and reactive output power P_g and Q_g can be calculated based on v_{cd}, v_{cq}, i_{id}, and i_{iq} through using the following equations [13]:

$$P_g = v_{cd}i_{id} + v_{cq}i_{iq}, Q_g = v_{cq}i_{id} - v_{cd}i_{iq}. \tag{16}$$

The system frequency f_g is obtained from the output of the PLL. All the references, i.e., P_{ref}, Q_{ref}, and V_{cref}, are application specific. Inside the frequency/power controller, the control parameters of the secondary frequency controller, frequency droop, speed governor, reheat turbine, inertia and damping unit, and reactive power controller can be selected based on the conventional power system frequency regulation model, which are detailed in [15]. Among these control blocks, the inertia and damping unit describes the well-known swing equation, and it can be expressed in the per-unit form as follows:

$$P_{in\_pu} - P_{g\_pu} = 2H_i \frac{df_{o\_pu}}{dt} + D_i\Delta f_{o\_pu}, \tag{17}$$

where P_{in_pu} and P_{g_pu} respectively denote the input power and output power of the VSG. $H_i = J\omega_{ref}^2 / (2VA_{ref})$ represents the inertia coefficient, J stands for the combined moment of inertia of the generator and turbine, ω_{ref} is the rated angular frequency, and VA_{ref} is the base power rating. Δf_{o_pu} denotes the output frequency deviation, D_i represents the damping coefficient, and a frequency droop coefficient $R_d = 0.05$ is used. It means that a 5% frequency deviation will cause a 100% output power deviation. The secondary frequency controller is optional, which will be activated by an upper level control if necessary. It is implemented as an integrator in this study:

$$K_{fi}(s) = \frac{K_{fi}}{s}. \tag{18}$$

The transfer functions of the speed governor and reheat turbine are the same as those used in [15]. The reactive power controller can be configured as either voltage control mode or reactive power control mode, and it is operated in the voltage control mode here. The f to ωt unit converts the output frequency f_o into the phase angle $\omega_o t$, which is later used as a reference for the voltage/current controller. Based on the parameter values of the frequency/power controller listed in

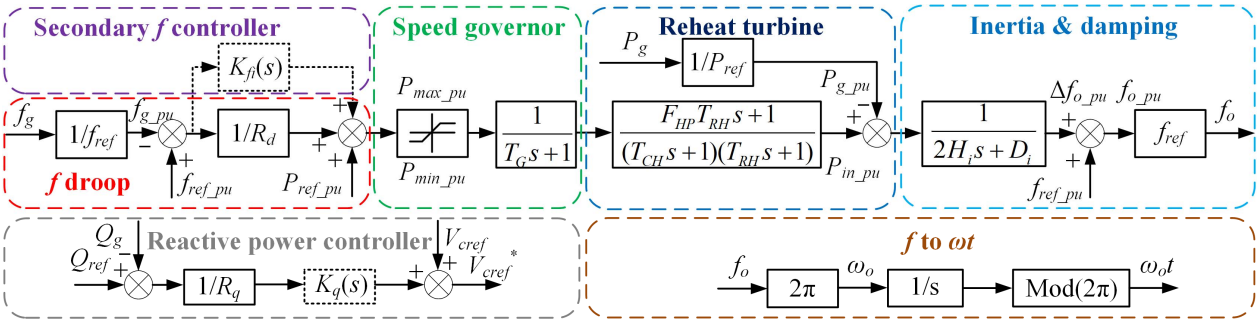

Fig. 12. Control block diagram of the frequency/power controller.

Table III, the zero-pole map of the transfer function from the load disturbance $P_{g\_pu}(s)$ to the frequency deviation $\Delta f_{o\_pu}(s)$ is shown in Fig. 13. As observed, although the increase of the secondary frequency controller integral gain K_{fi} will reduce the stable margin, the system would always be stable. It should be mentioned that these control parameter values can easily be tuned under various power system operating conditions.

V. Experimental Verification

Experiments on the proposed VSG have been carried out based on the system schematic diagram shown in Fig. 1 and parameters listed in Tables I–III. A photo of the experimental prototype is illustrated in Fig. 14. As seen, the control algorithm was executed by a dSPACE control platform (dSPACE: microlabbox). Litz wires with low equivalent-series-resistors (ESRs) were used as inductor windings.

The experimental waveforms of the VSG with two groups of current control parameter values are illustrated in Fig. 15. As seen, the AC output voltages v_x ($x = a, b, c$) can be regulated as clean sinusoidal waveforms when the proposed controller is

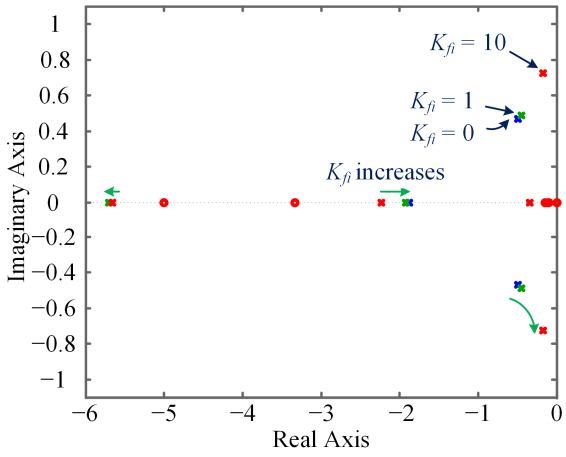

Fig. 13. Zero-pole map of $\Delta f_{ou}(s) / P_{gu}(s)$ with various K_{fi}.

Table III. Frequency/power controller parameter values.

Description	Symbol	Value
Fundamental frequency	f_{ref}	50 Hz
Droop coefficients	R_d / R_q	0.05 / 20
Active power reference	P_{ref}	500 W
Maximum active power	P_{max}	1000 W
Minimum active power	P_{min}	0 W
Speed governor coefficient	T_G	0.2 s
Turbine HP coefficient	F_{HP}	0.3
Time constant of main inlet	T_{CH}	0.3 s
Time constant of reheater	T_{RH}	7.0 s
Inertia coefficient	H_i	5.0
Secondary coefficient	K_{fi}	1.0
Damping coefficient	D_i	1.0

employed, i.e., $D_{if}K_i = 4$. After changing $D_{if}K_i$ into 8, the system becomes marginally stable, which is consistent with Fig. 5, verifying the damping effect of the voltage/current controller. Fig. 16 presents the experimental results of the VSG supplying a nonlinear load, which is composed of an inductor-filtered three-phase diode rectifier together with a resistive-capacitive load. Although the load current is seriously distorted with its THD value as high as 48.59%, the waveforms of AC voltages remain to be sinusoidal. Thanks to the help of the repetitive controller, the THD values of v_x ($x = a, b, c$) can be regulated as low as 1.39%. Furthermore, the integrator allows the steady-state error of voltage control at f_{ref} to be less than 0.3%. This indicates the effectiveness of voltage control.

Fig 17 demonstrates the primary frequency regulation capability of the VSG when the secondary frequency controller is disabled. To illustrate the effectiveness of the proposed frequency controller, the simulation results of the conventional synchronous generators are shown in Fig. 17(a), and the experimental waveform of the VSG is shown in Fig. 17(b). A

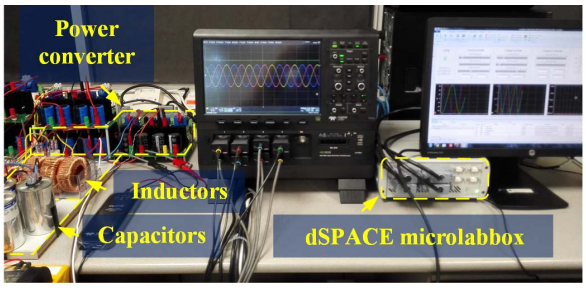

Fig. 14. A photo of the experimental prototype.

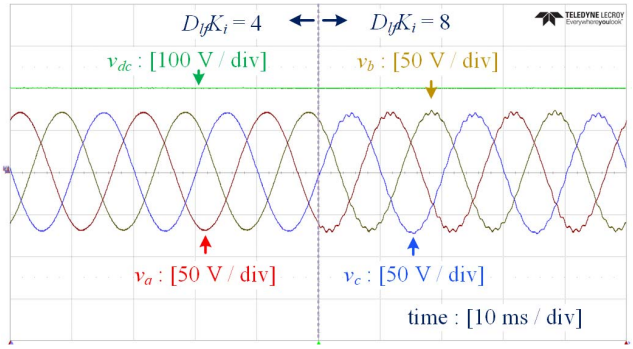

Fig. 15. Experimental waveforms of the VSG with two groups of current control parameter values ($D_{if}K_i = 4$ and $D_{if}K_i = 8$).

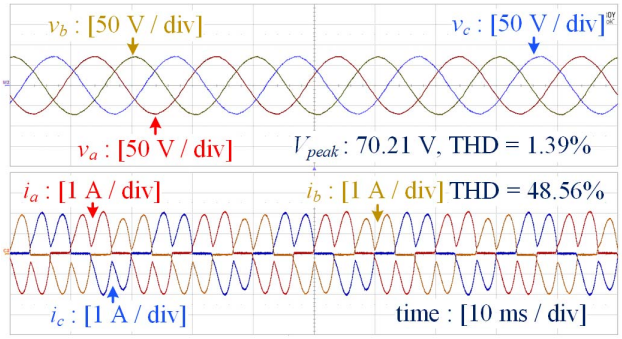

Fig. 16. Experimental waveforms of the VSG supplying a nonlinear load.

5% step-down load change occurs at time t_1, and then it recovers at time t_2. As observed, the proposed VSG behaves the same as synchronous generators under load disturbances. Therefore, the analysis and design methods used in traditional power systems can be applicable to the modern power systems dominated by VSGs. Fig. 18 presents the frequency responses of the VSG when the secondary frequency controller is activated. In this case, the frequency restoration can be achieved, which agrees well with the theoretical analysis.

VI. Conclusion

This paper has detailed the design of virtual synchronous generators with enhanced frequency regulation and reduced voltage distortions. The proposed control structure consists of an inner-loop voltage/current controller as well as an outer-loop frequency/power controller. The inner-loop controller allows effective damping of the resonance introduced by the output *LC*-filter while maintaining a high-quality voltage support even for nonlinear loads. The outer-loop frequency and power controller enables VSGs to exhibit the same inertial frequency responses, e.g., primary and secondary frequency regulations, as conventional synchronous generators under frequency disturbances. Finally, experimental results obtained from a 500-W three-phase VSG prototype were presented to indicate the effectiveness of the proposed design method.

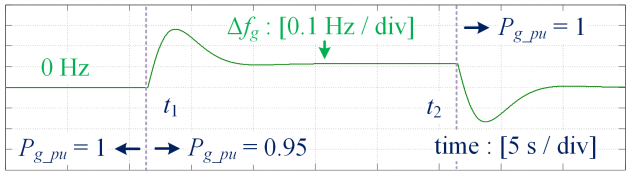

(a) Simulation waveform

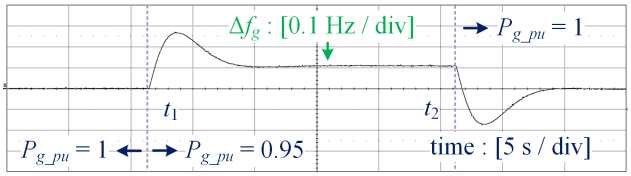

(b) Experimental waveform

Fig. 17. Primary frequency control of the VSG under load disturbances.

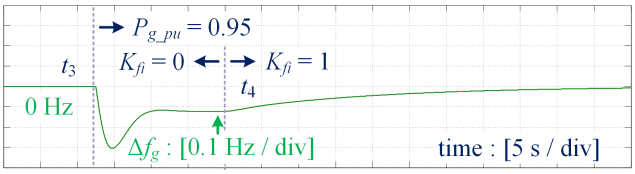

(a) Simulation waveform

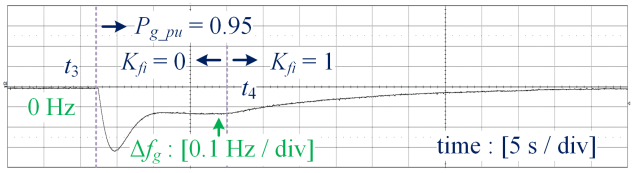

(b) Experimental waveform

Fig. 18. Secondary frequency control of the VSG under load disturbances.

Acknowledgment

This research is supported by the National Research Foundation, Prime Minister's Office, Singapore under the Energy Programme and administrated by the Energy Market Authority (EP Award No. NRF2015EWT-EIRP002-007)

References

[1] F. Blaabjerg, R. Teodorescu, M. Liserre, and A. V. Timbus, "Overview of control and grid synchronization for distributed power generation systems," *IEEE Trans. Ind. Electron.*, vol. 53, DOI 10.1109/TIE.2006.881997, no. 5, pp. 1398–1409, Oct. 2006.

[2] J. Fang, X. Li, X. Yang, and Y. Tang, "An integrated trap-*LCL* filter with reduced current harmonics for grid-connected converters under weak grid conditions," *IEEE Trans. Power Electron.*, vol. 32, DOI 10.1109/TPEL.2017.2651152, no. 11, pp. 8446–8457, Nov. 2017.

[3] J. Rocabert, A. Luna, F. Blaabjerg, and P. Rodriguez, "Control of power converters in AC microgrids," *IEEE Trans. Power Electron.*, vol. 27, DOI 10.1109/TPEL.2012.2199334, no. 11, pp. 4734–4749, Nov. 2012.

[4] G. Delille, B. Francois, and G. Malarange, "Dynamic frequency control support by energy storage to reduce the impact of wind and solar generation on isolated power system's inertia," *IEEE Trans. Sustain. Energy*, vol. 3, DOI 10.1109/TSTE.2012.2205025, no. 4, pp. 931–939, Oct. 2012.

[5] J. Driesen and K. Visscher, "Virtual synchronous generators," in *Proc.* IEEE Power Energy Soc. Gen. Meeting–Conversion and Delivery of Electrical Energy in the 21st Century, DOI 10.1109/PES.2008.45968000, pp. 1–3, Jul. 2008.

[6] H.-P. Beck and R. Hesse, "Virtual synchronous machine," in *Proc. 9th Int. Conf. EPQU*, DOI 10.1109/EPQU.2007.4424220, pp. 1–6, 2007.

[7] Q.-C. Zhong and G. Weiss, "Synchronverters: Inverters that mimic synchronous generators," *IEEE Trans. Ind. Electron.*, vol. 58, DOI 10.1109/TIE.2010.2048839, no. 4, pp. 1259–1267, Apr. 2011.

[8] S. D'Arco and J. A. Suul, "Equivalence of virtual synchronous machines and frequency-droops for converter-based microgrids," *IEEE Trans. Smart Grid*, vol. 5, DOI 10.1109/TSG.2013.2288000, no. 1, pp. 394–395, Jan. 2014.

[9] J. Liu, Y. Miura, and T. Ise, "Comparison of dynamic characteristics between virtual synchronous generator and droop control in inverter-based distributed generators," *IEEE Trans. Power Electron.*, vol. 31, DOI 10.1109/TPEL.2015.2465852, no. 5, pp. 3600–3611, May. 2016.

[10] Y. Hirase, K. Sugimoto, K. Sakimoto, and T. Ise, "Analysis of resonance in microgrids and effects of system frequency stabilization using a virtual synchronous generator," *IEEE J. Emerg. Sel. Topics Power Electron.*, vol. 4, DOI 10.1109/JESTPE.2016.2581818, no. 4, pp. 1287–1298, Jun. 2016.

[11] J. Fang, Y. Tang, H. Li, and X. Li, "A battery/ultracapacitor hybrid energy storage system for implementing the power management of virtual synchronous generator," *IEEE Trans. Power Electron.*, to be published.

[12] Q.-C. Zhong, P.-L. Nguyen, Z. Ma, and W. Sheng, "Self-synchronized synchronverters: inverters without a dedicated synchronization unit," *IEEE Trans. Power Electron.*, vol. 29, DOI 10.1109/TPEL.2013.2258684, no. 2, pp. 617–630, Feb. 2014.

[13] H. Akagi, Y. Kanazawa, and A. Nabae, "Instantaneous reactive power compensators comprising switching devices without energy storage components," *IEEE Trans. Ind. Appl.*, vol. 20, DOI 10.1109/TIA.1984.4504460, no. 3, pp. 625–630, May/Jun. 1984.

[14] K. Zhang, Y. Kang, J. Xiong, and J. Chen, "Direct repetitive control of SPWM inverter for UPS purpose," *IEEE Trans. Power Electron.*, vol. 18, DOI 10.1109/TPEL.2003.810846, no. 3, pp. 784–792, Mar. 2003.

[15] P. Kundur, *Power System Stability and Control*. New York, NY, USA: McGraw-Hill, pp. 598-601, 1994.